HHS Public Access

Author manuscript

ACS Nano. Author manuscript; available in PMC 2022 July 11.

Published in final edited form as:

ACS Nano. 2018 July 24; 12(7): 6597–6611. doi:10.1021/acsnano.8b01424.

Vascular Interventional Radiology-Guided Photothermal Therapy of Colorectal Cancer Liver Metastasis with Theranostic Gold Nanorods

Abdul Kareem Parchur[†], **Gayatri Sharma**[†], **Jaidip M. Jagtap**[†], **Venkateswara Rao Gogineni**[‡], **Peter S. LaViolette**[‡], **Michael J. Flister**[§], **Sarah Beth White**[‡], **Amit Joshi**[*,†,‡]

[†]Department of Biomedical Engineering, Medical College of Wisconsin, Milwaukee, Wisconsin 53226, United States

[‡]Department of Radiology, Medical College of Wisconsin, Milwaukee, Wisconsin 53226, United States

[§]Department of Physiology, Medical College of Wisconsin, Milwaukee, Wisconsin 53226, United States

Abstract

We report sub-100 nm optical/magnetic resonance (MR)/X-ray contrast-bearing theranostic nanoparticles (TNPs) for interventional image-guided photothermal therapy (PTT) of solid tumors. TNPs were composed of Au@Gd_2O_3:Ln (Ln = Yb/Er) with X-ray contrast (~486 HU; 10^{14} NPs/mL, 0.167 nM) and MR contrast (~1.1×10^8 mM^{-1} S^{-1} at 9.4 T field strength). Although TNPs are deposited in tumors following systemic administration *via* enhanced permeation and retention effect, the delivered dose to tumors is typically low; this can adversely impact the efficacy of PTT. To overcome this limitation, we investigated the feasibility of site-selective hepatic image-guided delivery of TNPs in rats bearing colorectal liver metastasis (CRLM). The mesenteric vein of tumor-bearing rats was catheterized, and TNPs were infused into the liver by accessing the portal vein for site-selective delivery. The uptake of TNPs with hepatic delivery was compared with systemic administration. MR imaging confirmed that delivery *via* the hepatic portal vein can double the CRLM tumor-to-liver contrast compared with systemic administration. Photothermal ablation was performed by inserting a 100 μm fiber-optic carrying 808 nm light *via* a JB1, 3-French catheter for 3 min under DynaCT image guidance. Histological analysis revealed that the thermal damage was largely confined to the tumor region with minimal damage to the adjacent liver tissue. Transmission electron microscopy imaging validated the stability of core−shell structure of TNPs *in vivo* pre- and post-PTT. TNPs comprising Gd-shell-coated

[*]**Corresponding Author:** Phone: +1-(414) 955-7588. Fax: +1-(414) 805-8282. ajoshi@mcw.edu.

ASSOCIATED CONTENT

Supporting Information

The Supporting Information is available free of charge on the ACSPublicationswebsite at DOI: 10.1021/acsnano.8b01424.

Additional TEM images of TNPs, temperature kinetics of TNP-mediated photothermal ablation, illustration of fluoroscopic guidance for selecting vessels for administration of TNPs, weight changes in PTT-treated CRLM-bearing rats, and ICP-MS spectroscopy-based Au and Gd distribution at log scale for clearly depicting metal retention in low accumulating organs (PDF)

The authors declare no competing financial interest.

Au nanorods can be effectively employed for the site-directed PTT of CRLM by leveraging interventional radiology methods.

Keywords

colorectal cancer liver metastasis; image-guided interventional therapy; laser ablation; MR contrast; X-ray contrast; gold nanorods

The American Cancer Society estimates that approximately 1 in 24 Americans will be diagnosed with colorectal cancer (CRC) in their lifetime. About 724,690 men and 727,350 women in the U.S. were suffering from CRC as of January 1, 2016 and need effective treatment options for this debilitating condition. Although the cancer survival rate has slightly increased since 1975, still 135,430 new CRC cases and 50,260 deaths occurred in 2017.[1,2] Nineteen percent of CRC patients have synchronous metastasis, with the liver being the most common site of metastatic spread.[3] However, more than 70% of patients with colorectal liver metastases (CRLM) are not eligible for surgical resection due to inaccessible location, size, bilobar distribution of their hepatic metastases, circumferential resection margins, and/or the volume of future liver remnant postsurgery.[4] Of those undergoing potentially curative hepatic resection, only a 50% rate of survival at 5 years was achieved.[5] Although the devastating nature of metastatic unresectable liver tumors has been recognized, systemic therapeutics continues to be the only treatment option recognized for first-line therapy. Therefore, patients are offered multiple lines of chemotherapy, which are poorly tolerated and ineffective (5 year survival rate is <5%).

Local ablation therapies are increasingly employed for treating nonresectable solid tumors in the liver, including (i) cryoablation, (ii) high-intensity focused ultrasound, (iii) radio frequency (RF) ablation, (iv) microwave ablation, (v) irreversible electroporation, and (vi) laser ablation. These procedures are preferred due to minimal pain and a recovery time shorter than that with surgery. Further, these procedures do not require an overnight hospital stay. A recent study of 14,150 CRLM patients indicated that liver-directed therapies (LDT), including various ablative modalities, provided a strong survival benefit with a 26.9% 5 year overall survival achieved for those undergoing LDT and 7.5% who did not.[6] Although these local ablative techniques have made great strides in the palliative treatment of CRLM since their introduction, they are also limited by the size and location of tumors and have additional off-target effects such as bile duct or vascular injury due to the percutaneous insertion and nonspecific heating by ablative probes. Several clinical trials have evaluated the effectiveness of different ablation methods without a clear consensus.[7,8] Conventional ablation methods including microwave, RF, or cryoablation do not discriminate between tumors and normal tissue and critically depend on operator skill in placing the ablative probe for a successful outcome; thus, conflicting efficacy results have been reported in the literature.[9] A wide implementation of chemo- or radioembolization therapy is also limited due to dose-limiting toxicity, difficulty in site-selective delivery, and size and location of the tumor. Therefore, there is a pressing need for effective tumor-selective interventional radiology-guided liver cancer therapies.

Nanomedicine developments in the past two decades have resulted in numerous theranostic probes for both imaging and/or therapy delivery to solid tumors.[10,11] Although nanoparticles (NPs) are deposited in tumors following systemic administration *via* enhanced permeation and retention (EPR) effect, the delivered dose to tumors is typically low, and a majority of the NPs are excreted by the reticuloendothelial system (Kupffer cells and macrophages) from the systemic circulation within a few hours.[12−14] Further, the NPs' circulation velocity is reduced by 1000× in the liver, leading to extensive nonspecific deposition.[15] In general, for solid tumors, only a small fraction of NPs (~0.7% injected dose (ID)) overcomes the transport and biological barriers and interacts with tumor tissue, a figure which can be further reduced for liver tumors due to nonspecific uptake.[14,16] Enhancement in %ID *via* active targeting strategies such as by molecularly targeting the tumor by ligand conjugation has been reported to increase the delivery efficiency by only less than 0.3%.[14] The low tumor uptake efficiency of NPs following systemic delivery has adverse implications for clinical translation due to long-term toxicity concerns caused by 99% of ID being off-target. Multiple nanomedicine engineering approaches have been attempted to increase the tumor dose, including the use of (i) sub-100 nm particle size, (ii) neutral ζ-potential (ζ = −10 to +10 mV), and (iii) rod or linear NP shape.[14] Although these approaches modestly increase the tumor dose, local vascular delivery in a tumor in a site-directed manner dramatically enhances NP accumulation in tumors and provides clinical translational routes for multiple diseases, especially in diseases where interventional radiology-guided ablation and chemoembolization are standard of care treatments. Interventional radiology-based methods employing radio-opaque emulsion Lipiodol have been reported for locally enhanced Au NP deposition in liver tumors. A tumor dose significantly higher (~4.1 ± 0.6-fold higher) than that with a normal liver has been shown for ~45 nm PEGylated hollow Au nanospheres (ζ = −16 mV) loaded in Lipiodol and delivered through intra-arterial injection in a rabbit VX2 liver tumor model.[17,18] White *et al.* also demonstrated effective photothermal ablation of hybrid magnetic Au-nanosphere-tagged colorectal liver metastasis albeit by a percutaneously implanted optical fiber laser source in the tumor.[19] These interventional image-guided procedures with laser ablation relied on nonspecific contrast-enhanced tagging of tumors with radio-opaque agents for placing ablation probes and assigning ablation settings based on imageable tumor dimensions. However, these methods are constrained by heterogeneity in tumor contrast and low sensitivity of fluoroscopic or cone beam computed tomography (CT) imaging for soft tissue tumor delineation, leading to under- or overtreatment. The soft tissue contrast limitations of X-ray imaging have motivated the advances in magnetic resonance (MR) imaging for tumor characterization and delineation for therapy planning, further supported by large-cohort comparative studies (>3000 patients) concluding that MR contrast sensitivity is higher than that of CT for therapy planning.[20] Development of theranostic probes that integrate MR and X-ray contrasts with therapeutic remote-triggered NPs can dramatically streamline the interventional radiology workflow and improve tumor accumulation and therapy response when delivered in an image-guided and site-directed manner. Multiple conjugates of Au NPs and iron oxide NPs for potential use as MR image-guided agents[21−24] have been reported, but it is difficult to clearly distinguish tumor and nontumor regions through T_2-weighted MR contrast. Other researchers have reported chelated Gd(III) agents conjugated to Au NPs for the T_1-weighted MR imaging of NP delivery, but site-directed liver tumor treatment has

not been demonstrated.[25−29] A major disadvantage of Au-NP-chelated Gd(III) agents is the potential decomposition of conjugates *in vivo*, leading to the release of free Gd(III) chelate with dramatically different circulation half-life and clearance pathways, and release of free Gd(III) to nontargeted organs is increasingly being recognized and reported in diverse applications of contrast-enhanced MR imaging (MRI).[30] To create robust Au NPs with a safe T_1-weighted Gd(III)-based MR contrast, Marangonia *et al.* recently reported a layered nanoconstruct, where chelated Gd(III) ions were incorporated onto a SiO_2 layer between a Au core (50 nm) and Au shell (13−38 nm), ensuring the stability of the Gd(III) contrast and consistency of clearance and circulation of NPs and Gd(III) contrast. However, no *in vivo* experiments were performed or reported with these Gd(III) nanomatryoshkas.[31] Alternative MR-visible and stable constructs, which do not employ chelated Gd(III), can be created *via* controlled lanthanide oxide/fluoride deposition on near-infrared (NIR) resonant Au nanorods (GNRs) for MR image-guided PTT. Coating with inorganic Gd(III)-based shells[32−35] can also restrict the temperature-sensitive shape deformation of GNRs, wherein GNRs lose their NIR resonance and therapeutic ability and potentially change the clearance profile on interaction with NIR light even at low bulk temperatures (below the melting point of Au).[36] These stable inorganic shells bearing GNR-based theranostic NPs (TNPs) provide a robust solution to MR and X-ray-guided site-directed treatment of liver tumors, but the synthesis and characterization of such TNPs at volumes large enough for proof-of-concept animal studies, evaluation of multimodal contrast, and therapy efficacy have not been investigated or reported.

Here, we report a scale-up synthesis of TNPs based on Gd_2O_3-coated GNRs with Yb/Er doping and biofunctionalization for image-guided biodistribution studies on ~300−350 g Wistar rats bearing CRLM tumors. We further report a direct comparison of the dose uptake of TNPs *via* systemic administration *versus* hepatic portal vein delivery methods in CRLM-bearing rats and demonstrate the feasibility of liver-tumor-directed vascular photothermal therapy (PTT). The primary purpose of this study was to demonstrate a proof-of-concept for an efficient hepatic site-selective delivery of trimodal optical/MR/X-ray contrast-bearing TNPs by a minor modification of the existing interventional image-guided clinical procedures. To the best of our knowledge, this study is the first to demonstrate highly stable TNPs with a GNR core and inorganic Gd(III) layer that retain shape and ablative capability over multiple cycles and are stable *in vivo*, while providing usable MR and CT contrasts on clinical scanners for clearly visualizing CRLM tumors. MR imaging revealed a detailed picture of the distribution of TNPs in CRLM tumors and enabled a noninvasive comparison of local *versus* systemic delivery routes, whereas X-ray imaging guided the site-directed delivery of TNPs and therapeutic light to CRLM tumors. *Ex vivo* histology verified the specific ablation of TNP-tagged tumor tissue at low levels of light, which did not affect the non-TNP-tagged tissue, whereas scanning transmission electron microscopy (STEM) imaging validated the stability of TNPs *in vivo* with and without NIR light excitation and resulted in photothermal heating.

RESULTS AND DISCUSSION

Synthesis and Characterization of TNPs.

The overall strategy for treating CRLM tumors with interventional image-guided site-selective delivery of TNPs directly to the liver circulation *via* portal vein/hepatic artery is illustrated in Figure 1. The TNPs have a core−shell structure with NIR plasmonresonant GNRs as the core and a Gd(III) inorganic layer as the shell. The synthesis scheme of TNPs is illustrated in Figure 2A. PEGylated TNPs were synthesized with the controlled growth of a lanthanide oxide shell, while keeping the overall size under 100 nm and in batch sizes large enough for *in vivo* experiments on ~350 g rats.[33,35] We first synthesized hexadecyltrimethylammonium bromide (CTAB)-coated GNRs (GNR-CTAB) *via* an established method by the El-Sayed group,[37] followed by sodium oleate (NaOA) coating, facilitating the formation of a uniform gadolinium oxide shell in the presence of hexamethylenetetramine (HMT). NPs with a size of sub-100 nm are regarded as an ideal platform for cancer treatment because small particles (<10 nm) are quickly excreted by the kidneys and large particles (>100 nm) are rapidly cleared by the immune system. The successful coating of the gadolinium shell onto the surface of GNRs was confirmed by both STEM and TEM images, as shown in Figures 2B and S1, respectively. The average size of TNPs was ~75 nm in diameter. The thickness of the shell was tuned by controlling the concentration of the Gd precursor, reaction time (up to 6 h), and temperature (80−120 °C) during the synthesis. To verify the elemental composition of TNPs, ultrasensitive STEM and dual-energydispersive X-ray spectroscopy (EDS) elemental mapping for Au and Gd were conducted on single TNPs, as depicted in Figure 2B. The EDS spectrum of single TNPs establishing the physical elemental composition is depicted in Figure 2C, and no impurity phases were detected. A Si peak at 1.74 keV was generated from APTES coated on the surface TNPs and/or two Si-EDS detectors in dual-EDS Hitachi HD-2300A STEM, whereas a Cu peak at 8.05 keV was generated from the TEM grid. As the TNPs formed, it is essential to understand the surface plasmon resonance (SPR) properties for the effective PTT response to NIR light. The GNR-CTAB synthesized using a seed growth technique showed two plasmon absorption bands at (i) 515 nm (transverse mode) and (ii) 830 nm (longitudinal mode) related to GNRs with average dimensions of ~12 nm × 50 nm (width × length) with a full width at half-maximum (fwhm) of the longitudinal plasmon band at ~126.9 nm. NaOA functionalization onto GNRs resulted in a slight blue shift of the longitudinal plasmon band by ~12 nm, and its fwhm increased by ~18.3 nm. Furthermore, an increase in the fwhm of longitudinal plasmon peak of TNPs by 41.6 nm compared with that of the CTAB-functionalized GNRs was observed (Figure 2D). The longitudinal plasmon peak of TNPs exhibited a further slight blue shift (~3 nm) compared with that of NaOA-GNRs, and the fwhm increased by 23.3 nm, possibly due to a prolonged heating of GNRs at 120 °C for 3 h during the synthesis. Furthermore, to understand the effect of reaction temperature on the SPR properties of GNR-NaOA, reactions were carried out with and without the Gd precursor in the presence of HMT at 100 °C for 3 h. A blue shift in the SPR peak (~40 nm) was observed in the absence of a Gd precursor, whereas a red shift (~35 nm) was observed in the presence of a Gd precursor. Because of a strong NIR longitudinal plasmon band of TNPs and deep tissue penetration of NIR light, these nanoconstructs can be used for cancer PTT applications. One of the concerns with GNRs for PTT is the variable shape

stability of GNRs depending on temperature during NIR-light-triggered PTT, which changes the SPR and adversely affects further PTT. This effect can be alleviated by coating a thin inorganic shell such as SiO_2 on the surface of GNRs. Recently, Taylor *et al.*[38] confirmed the reshaping mechanism of GNRs both theoretically and experimentally and attributed the mechanism to the surface diffusion of Au atoms instead of temperature-dependent phase change or melting. Thus, it is important to modify and stabilize the geometry of GNRs for cancer PTT applications by maintaining their shape, size, and SPR properties intact, not only for PTT efficacy but also for controlling the size/shape-dependent *in vivo* clearance profiles. Next, we modified the surface of TNPs and functionalized *via* the following successive surface conjugation steps: First, an "NH_2 group" was grafted onto TNPs using 3-aminopropyltriethoxysilane (APTES). The successful functionalization of the $-NH_2$ group onto TNPs was confirmed by an increase in the ζ-potential from +25 to +29 mV. Second, the COOH group of mPEG-COOH was reacted with the NH_2 group on TNPs to form biocompatible near-neutral surface charge theranostic particles (+6.2 mV). The variation in the surface charge of TNPs is depicted in Figure 2E. These near-neutral PEGylated TNPs demonstrate EPR-dependent uptake in tumors due to their extended blood circulation. The inset of Figure 2E depicts the NIR-II emission of TNPs using dual 980 nm diode laser excitation from both sides of a quartz cuvette and emission measured at 1530 nm. The digital photographs of aqueous solutions of GNR-CTAB, GNR-NaOA, and TNP-mPEG with a concentration of ~10^{11} NP/mL dispersed in water are depicted in Figure S2.

Photothermal Properties of TNPs.

The photothermal potential and temperature stability of TNPs were characterized in cuvette phantoms simulating *in vivo* conditions with an 808 nm NIR laser diode source. Figure 3A depicts that the maximum change in temperature (ΔT_{max} in °C) for TNP-mPEG (10^{11} NPs/mL) rapidly increased with NIR irradiation power. At 0.7, 1.0, and 1.5 W/cm^2 exposures for 3 min, ΔT_{max} reached 12, 19, and 29 °C, respectively. Under the same conditions, no significant change was observed (ΔT_{max} = 2−5 °C) for an equal volume of 0.9% saline solution. These results indicate that therapeutically pertinent ΔT_{max} depended on the concentration of TNPs, and physiologically safe power density levels of NIR light were delivered. These results also show that the *in vivo* tumor PTT efficacy critically depends on the TNP uptake or percentage ID of TNPs (%ID) in tumors. Forward-looking infrared (FLIR) thermal images of a quartz cuvette containing saline or TNPs at different time points between 0 and 5 min at 1.5 W/cm^2 irradiation is depicted in Figure 3B. To assess the photostability of TNPs, five cycles of ON/OFF 2 W/cm^2 NIR laser irradiations (6 min ON and 24 min OFF) were performed. The results are shown in Figure 3C, consistent with ΔT_{max}, thus highlighting the stability of TNPs for *in vivo* PTT applications. Next, we evaluated the PTT transduction efficiency of TNPs using the following formula:

$$\eta = \frac{hA(T_{max} - T_{amb}) - Q_0}{I(1 - 10^{-OD})}$$

where h is the heat transfer coefficient, A is the sample surface area, T_{max} is the steady-state maximum temperature, T_{amb} is the ambient room temperature, Q_0 is the baseline energy

input by the solvent and sample cell without NPs, I is the NIR laser power density, and OD is the optical density of TNPs at the laser wavelength.[39] The photothermal transduction efficiency of TNPs was 55.7% (Figure S3). These results confirm that, although there is some loss of PTT efficiency compared to that with bare GNRs,[40] the PTT efficacy is sufficient for TNPs with an additional gain of multimodal image contrasts and temperature cycling stability.

X-ray and MR Contrasts of TNPs.

GNRs have gained attention as a CT contrast agent because of their high X-ray attenuation, colloidal stability, easy surface functionalization, and targeted tumor delivery. TNPs consist of both Au and Ln(III) ions with a high atomic number; Au (K-edge = 80.7 keV), Gd (K-edge = 50.2 keV), and Yb (K-edge = 61.3 keV) as the major constituents and Er (K-edge = 59.3 keV) as the minor constituent that attenuate X-rays because of their large absorption cross sections. To examine the X-ray contrast capability of TNPs, a CT phantom was prepared by varying the concentration of TNPs between 0 and 30×10^{13} NP/mL (49.8×10^{-8} mM) in water, and the mean linear attenuation coefficient was measured in Hounsfield unit (HU) at 80 kV, as depicted in Figure 4A,B. The X-ray attenuation of TNPs linearly increased with the increase in mass concentration. A linear fit to HU values and TNP concentration is illustrated in Figure 4B. Typically, 10^{14} NPs/mL TNPs (0.167 nM) exhibited an X-ray attenuation of 486 HU. These results indicate that TNPs can be used as a CT contrast agent for *in vivo* applications, especially for tumor site-directed delivery, where higher TNP doses can be easily delivered.

To evaluate the longitudinal relaxation of TNPs in MRI scanners, T1MR mapping was performed using a 9.4 T small animal MRI scanner. The T_1-weighted images corresponding to different concentrations of TNPs varying from 0 to 7.5×10^{12} NP/mL (1.25×10^{-8} mM) are depicted in Figure 4C,D; $1/T_1$ *versus* TNP concentration plots confirmed the linear dose-dependent T1MR contrast enhancement with longitudinal relaxivity, $r_1 = 1.1 \times 10^8$ mM^{-1} s^{-1} per TNPs, and transverse relaxivity, $r_2 = 4.8 \times 10^8$ mM^{-1} s^{-1} per TNPs (*i.e.*, $r_1/r_2 = 0.23$). Recently, in comparable constructs, Nicholls *et al.* conjugated Gd(III) to 15.3 nm spherical Au NPs and reported $r_1/r_2 = 0.37$. Because the DNA−Gd(III)−HPDO3A molecules were conjugated to the surface of Au, some cumulative loss of Gd(III) of 0.5−5% occurred.[28] However, as our TNPs are coated with an inorganic Gd(III) shell at 120 °C, almost no cumulative loss occurred compared with covalently functionalized chelated contrast molecules. The effective number of Gd(III) molecules directly interacting with the surrounding water molecules affects the r_1 relaxation.[31] An Au nanomatryoshka system (Au−SiO_2−Au construct) was recently studied both experimentally and theoretically, where Gd(III) ions were incorporated into an interstitial silica layer, and the thickness of the Au shell was varied (Solomon−Bloembergen−Morgan theory).[31] In another study, Rotz *et al.* synthesized Au stars heavily decorated with Gd(III) molecules; the relaxivity was significantly enhanced because of more interaction of chelated Gd(III) molecules with the surrounding water molecules.[25] The relaxivity can be easily tuned by changing the thickness of the Gd(III) shell in our current TNP systems by changing the amount of inorganic precursor during the nucleation, with the advantage that no cumulative loss can be expected

with NIR light delivery and therapy because of the absence of chelated Gd(III) covalent conjugation.

In Vivo MR Imaging.

T_1-weighted MR imaging has been extensively used for the detection and characterization of tumors, scars, and focused fibrosis in the clinic; however, there is a paucity of multifunctional theranostic nanovehicles capable of guiding clinical interventional procedures. The Au core lanthanide shell TNPs were tested for the imaging and potential thermal treatment of CRLM tumors in an immunocompetent rat strain in both systemic and site-specific delivery settings. After successful liver tumor inoculation in six ~350 g Wistar rats, three rats were tail-vein-catheterized for systemic administration of TNPs, and the remaining three rats were catheterized *via* hepatic portal vein (site-selective injection). Site-specific catheter-driven delivery to hepatic circulation was meant to be immediately followed by catheter-based NIR light delivery for ablation; thus, it is important to identify delivery protocols that maximize the tumor to normal liver dose. The T1MR contrast of TNPs allowed a direct comparison of tumor %ID for systemic (tail vein) and interventional (hepatic portal vein) routes. The T_1-weighted MR images of rats with CRLM tumors for pre- (0 h), post-4 h, and post-24 h systemic administration and pre- (0 h) and post-5 min hepatic portal vein injection of TNPs are depicted in Figure 5A,B. The objective of comparing MR contrast in both systemic and portal vein routes is to verify that the local liver vascular injection indeed achieves a higher tumor-to-normal liver ratio in the timeframes involved in IR procedures, whereas at conventional time points ranging from 4 to 24 h used for PTT following systemic delivery, the tumor-to-normal liver distribution is not favorable for liver tumor ablation while minimizing the normal tissue injury. The tumor area is marked with a white boundary in the figure. In both cases, the T1MR images identified enhancement in CRLM tumors, but the absolute T1MR contrast was significantly higher for post-5 min hepatic portal vein injections, thus indicating the feasibility of TNP delivery and PTT in the same anesthesia session. The T1MR contrast of tumors in systemically injected rats increased with time, but the normal liver uptake increased, as well. In contrast, the tumor region was clearly distinguishable in the hepatic portal vein. This may be due to the gradual clearance of TNPs by the hepatocytes/sinusoidal space instead of fast clearance by the reticuloendothelial system.[41] The change in T1MR signal contrast was analyzed with MATLAB using 3−5 T_1-weighted MR images with 3−5 averages passing through the tumor in each rat at different time points. The CRLM tumor signal to background signal ratio (TBR) enhancement was calculated for each slice and averaged over all slices. TBR enhancement factor accounts for the intensity variation at different MR slice acquisitions relative to the background.[21] The TBR ratios at different time points of systemic administration and hepatic portal vein injection in rats are depicted in Figure 5C. For systemic delivery, the TBR enhancement increased by 33.2% at 4 h and then decreased to 15.1% at 24 h post-tail-vein injection, whereas 181.2% increment was observed in 5 min in tumors posthepatic portal vein administration. Statistical analysis *via* two-tailed homoscedastic *t*-test between post-4 h, post-24 h systemic administration and post-5 min hepatic portal vein injection concluded significant differences with p values of 0.0349 and 0.0377, respectively. TBR enhancement with hepatic portal vein delivery was 111% higher than that of the systemic administration at the 4 h time point. This confirms

that the hepatic portal vein delivery resulted in a greater tumor dose enhancement of ~2.1 times. The higher T1MR contrast in CLMR tumor tissue indicated a higher uptake of TNPs in liver tissue; this is quite advantageous for improving the therapeutic response. These results confirm the high sensitivity of TNPs as T_1-weighted MR imaging contrast agents and the significant advantages of site-specific delivery of therapeutic NPs to CRLM tumors. Although several studies have claimed dramatic increases in tumor uptake (>100%) of NPs following systemic delivery by various surface modifications (*e.g.*, PEGylation and molecular targeting), it is evident that the majority of systemically administered NPs still end up in the spleen, liver, and kidneys.[13] The high absolute and high tumor-to-normal TNP delivery to CRLM tumor lesions by site-specific delivery can significantly affect image-guided interventional therapies.

In Vivo Interventional Image-Guided TNP Delivery and Therapy Procedure Development.

As observed in the MR imaging studies, interventional image-guided site-specific TNP delivery offers the possibility of minimally invasive and effective treatment of CRLM. C-Arm fluoroscopy and cone beam DynaCT imaging are frequently used in the clinic during ablative therapies. We developed delivery and ablation procedures based on TNPs with X-ray imaging guidance provided by a clinical Siemens Artis-Zeego DynaCT system. TNPs were delivered through a catheter placed in a hepatic portal vein in three CRLM rats (Figure S4). The 3D reconstructed DynaCT image of a representative rat with a CRLM tumor and catheter placement in the portal vein is illustrated in Figure 6A. Following catheter placement, the rats were injected with TNPs followed by saline flush. Five minutes following TNP injection, NIR light was delivered. DynaCT images of rats (preinjection, post-TNPs, and post-PTT administrations) are shown in Figure 6B−D. Enhancement in the CT contrast of CRLM tumors confirms the uptake of TNPs in the CRLM tumor site. A 100 μm diameter optical fiber with a numerical aperture of 0.23 was inserted through the catheter to deliver NIR light to the tumor site (0.7 W/cm^2) for 3 min under DynaCT/fluoroscopy guidance. Post-PTT residual image enhancement was also observed, possibly because of local vascular ablation and trapping of TNPs. Inset of Figure 6A shows the dark-field image of CRLM tumor slice having TNPs; pointed arrows indicate scattering from TNPs, which confirms the uptake of TNPs. These procedures established the proof-of-concept of employing the vascular routes used for chemoembolization of tumors for delivering TNPs and therapeutic light to CRLM tumor sites.

In Vivo PTT Efficacy and TNP Stability.

Next, we examined the efficacy of NIR light PTT for ablating CRLM tumors after the delivery of TNPs through a hepatic portal vein under interventional image guidance. To clearly visualize the ablation region and photothermal temperature envelope *via* thermography, the procedure was carried out with the liver exposed, after placing the catheter for delivering TNPs in the portal vein. The liver tumors were directly exposed to 0.50 and 0.55 W/cm^2 (spot size 1.5 cm) for 5 min after the injection of TNPs (or saline for control) through a hepatic portal vein in CRLM tumor rats. Dynamic FLIR thermal imaging was performed during PTT (0.55 W/cm^2, 5 min exposure), and images at 0, 0.5, 1, 2, 3, 4, and 5 min time points are depicted in Figure 7A; the temperature kinetics profile is depicted in Figure S5A. CRLM tumor region of interest had an increase in temperature in

TNP-injected rats significantly higher than that of the control saline group. In the case of the saline group, the temperature of the CRLM tumor increased by ~7.5 °C in 1 min and then remained almost stable, whereas the TNP group tumor temperature rapidly increased up to ~19.5 °C in 5 min (0.55 W/cm^2). A stable temperature in the saline group with a continuous delivery of NIR light to the CRLM tumor illustrated that the photothermal heating was adequately convected by blood flow, and local tissue damage did not occur, as verified by a histopathological analysis. In the case of the TNP-injected group, the tumor temperature increased above the hyperthermia range, leading to the destruction of local vasculature and attainment of ablative temperature levels. This destroyed the CRLM tumor cells effectively. Further, to better understand the temperature distribution around the tumor and the effect on adjacent normal tissue with possible TNP uptake, a temperature line profile was drawn from the center of the tumor covering both normal liver tissue and the tumor region in both TNPs and saline groups, as depicted in Figure S5B. The results confirm that ΔT in the normal tissue region increased by ~2−3 °C in the TNP group, whereas no significant difference was observed in the case of the saline group. Both groups (saline and TNPs) in the normal liver region were in the normothermia regime, whereas only the TNP group tumors had irreversible hyperthermia and/or coagulation necrosis. To analyze the effect of thermal ablation, hematoxylin/eosin (H&E) staining of CRLM tumor sections was performed. As illustrated in Figure 7B, the tumor section of the saline group showed no apparent effect from NIR light at 0.5 and 0.55 W/cm^2, and no histopathological abnormalities were observed. This may be due to a low temperature increase (normothermia) under NIR laser irradiation (0.50 and 0.55 W/cm^2). The TNP group demonstrated an effective response with identical NIR laser irradiation power levels with a significant photothermal therapeutic effect. The ablation area was clearly visible in the CRLM tumor sections treated with TNPs and laser irradiation (0.50 and 0.55 W/cm^2). The ablation area also increased with increasing power of irradiation. A large and clear ablation zone with necrosis is visible in the tumor tissue treated with 0.55 W/cm^2 (marked with white arrows in Figure 7B) compared with the sections in rats treated with 0.50 W/cm^2. To visualize the uptake of TNPs in tumor microstructures and evaluate the stability with PTT, TEM imaging on CRLM sections was performed. The TEM images recorded at 70 kV confirmed that the TNPs remained in the tissue without any structural changes both pre-PTT and post-PTT, as depicted in Figure 7C. Furthermore, to clearly distinguish the core−shell structure of TNPs at pre-PTT and post-PTT, single-particle cryo-electron microscopy imaging was performed at 120 kV. This enabled the clear visualization of the morphology of a GNR core and a Gd(III) shell, as depicted in Figure 7D. The EDS spectrum confirmed the presence of both Gd and Au; that is, NIR light delivery to the CRLM tumor did not disturb the core−shell structure of TNPs. A shortwave infrared (SWIR) fluorescence emission image from the exposed liver of a Wistar rat locally injected at ~5 mm depth with 50 μL of TNPs with 10^{12} NPs/mL concentration under NIR excitation provided by two 980 nm laser diodes (200 mW) and imaged with a 980 nm notch-rejection filter and a 1550 ± 25 nm band-pass filter on a −60 °C thermoelectrically cooled InGaAs sensor equipped camera with 10 s exposure is depicted in Figure 7E, establishing the feasibility for intraoperative imaging-provided quantum yield and/or imaging sensitivity that can be further increased to decrease the exposure time requirement to under 1 s. These results indicate that TNPs can be

efficiently used for photothermal ablation without the risk of heat-induced TNP breakdown and resulting changes in size/shape-dependent clearance pathways.

In Vivo Hepatic PTT Impact on CRLM Tumor Response.

The effect of site-specific delivery and PTT on animal survival and tumor treatment was evaluated in three CRLM tumor-bearing rats. The rats were imaged with T_2-weighted MR imaging (echo time (TE) = 14.63 and repetition time (TR) = 1000 ms) to visualize the tumor contours. Tumor contours on T_2-weighted images were overlaid with thresholded T_1-weighted images (TE = 2.4 and TR = 100 ms) to evaluate the TNP-dependent enhancement in pre- and postinjection and therapy. TNP injections and PTT were performed under X-ray fluoroscopy guidance, as described in detail previously with 3 min treatment duration and 0.55−0.7 W/cm^2 power at the fiber tip. Figure 8A shows the thresholded T_1-weighted MR contrast over the T_2-weighted MR image of CRLM tumors at preinjection and post-48 h PTT. Compared to pretherapy tumors, the post-48 h tumor has more heterogeneity in the T_2 image due to the interventional PTT therapy treatment response. Furthermore, there is a slight increase in tumor volume in addition to heterogeneity in its structure; this is due to the swelling of the tumor (also called edema) in response to thermal therapeutic action from the NIR laser. Also, the tumor T_1 contrast at post-48 h therapy was 26.3% higher than that at pretherapy, probably because of retained TNPs. The weight fraction (weight of rat normalized to pretumor) suggests that post-therapy animal weight loss decreased in the first 0−3 days and then recovered by the fifth day (Figure S6). Thereon, animals were sacrificed if weight loss was observed: first animal at 6 days postprocedure, second at 9 days postprocedure, with the final animal maintaining weight and surviving until 18 days postprocedure when it was sacrificed to assess therapy. The postsacrifice tumor-bearing hepatic lobe was extracted, and the H&E stains were compared with those of an untreated control animal where CRLM tumors appear intact with no sign of necrosis, as shown in Figure 8B. In contrast, the representative H&E stain of CRLM tumors treated with TNPs and laser irradiation indicate extensive tumor necrosis and cell viability loss, as shown in Figure 8C. A large necrotic area in the center of the tumor tissue and damaged tissue at the periphery is clearly visible. This loss of tumor burden explains the survival time and weight maintenance in PTT-treated rats.

Biodistribution and Clearance of TNPs.

Two groups of rats with CRLM tumors (n = 6) and without tumors (n = 3) were systemically administered with TNPs. Urine and feces were carefully collected daily until the 10th day for a TNP excretion profile. On the 10th day, the animals were euthanized, and the brain, heart, kidneys, spleen, liver, lungs, tumor, colon, and blood were collected, rinsed with ultrapure water, and dried for TNP distribution for inductively coupled plasma mass spectrometry (ICP-MS) study. The tissues were dissolved for quantitative measurement of Au and Gd using the ICP-MS technique. The ICP-MS results confirm that majority of the particles were excreted more through feces than urine. The excretion kinetics of both Au and Gd in feces and urine until the 10th day of postsystemic administration of TNPs is depicted in Figure 9A,B. Higher fecal (or bile) excretion results support the previous biodistribution study, where about 100 nm silica particles were excreted *via* feces rather than urine.[42] These results suggest that TNP fecal (or bile) excretion plays a major role in the clearance

mechanism. Furthermore, the accumulation of Au and Gd in the major organs of rats on the 10th day of TNP postsystemic administration is depicted in Figure 9C,D, and its values at log scale are shown in Figure S7. The results show that the majority of NPs are cleared through feces/bile excretion, and in total, approximately only ~6% of the injected dose is retained in different organs. An average of 2.0 ± 0.08% of NPs was retained in the spleen, 3.5 ± 0.2% in the liver, and 1.7 ± 0.17% in the tumor at the 10th day postadministration. Moreover, a similar excretion trend was observed in both tumor- and non-tumor-bearing rats. Protein-to-creatinine ratio was used to evaluate renal function. We observed a mild increase in the protein-to-creatinine ratio in all the animals after 24 h (~1.3 ± 0.1), and it remained constant until the 10th day. For Wistar rats, the protein-to-creatinine ratio (a sensitive measure of proteinuria) of ~1 is considered as reflecting normal renal function; values over 20 are associated with renal dysfunction. A mild elevation of this ratio may indicate slight renal stress, or it may result from the contamination of urine samples with feces, which can happen in metabolic cages. However, histopathological study is valuable to detect any renal glomerulus degeneration or liver fibrosis and inflammation. The representative images depicting the histopathological features of the liver and kidney from animals with tumors and without tumors are shown in Figure 9E−H. As depicted in Figures 9E,F, the liver tissue of animals exposed to TNPs showed normal hepatocytes and overall normal morphological features. Also, Figure 9G,H depicts that there is no morphological change in the renal cortex. Glomerular cells, proximal and distal tubular cells, as well as extracellular matrix in kidneys of both groups of animals appear normal, and the animals did not indicate other markers of physiological stress with normal behavior, feeding, and weight gain.

CONCLUSIONS

PEGylated TNPs bearing optical/MR/X-ray contrasts were designed, characterized, and validated *in vivo*. TNPs consisted of a plasmonic GNR core epi-layered with a gadolinium oxide shell with consistent and controlled growth at a high temperature (120 °C). The gadolinium oxide shell can be doped with trace amounts of other lanthanides (Yb/Er) to create far-NIR luminescence upon NIR excitation. The TNPs had an X-ray contrast of 486 HU (10^{14} NPs/mL, 0.167 nM), MR contrast of 1.1×10^{8} mM^{-1} S^{-1} at 9.4 T field strength, and photothermal conversion efficiency of 55.7%. The TNPs were surface-functionalized to near-neutral charge for extended *in vivo* circulation. *In vivo* validation was performed in an immunocompetent syngeneic colorectal liver metastasis tumor-bearing rat model.

Theranostic NPs that are imageable with clinical X-ray and MR scanners and are capable of safe and tumor-specific ablation with a minor modification of established interventional chemo- or radioembolization protocols can substantially accelerate the clinical translation of emerging nanomedicine approaches. GNRs are established agents for efficient PTT solid tumors, but the lack of sensitive *in vivo* visualization of GNRs is a major challenge for dosing and therapy optimization. Although chelated Gd(III) agents have been covalently conjugated to GNRs for *in vivo* imaging,[43] the stability of such constructs *in vivo* is debatable. In particular, during the NIR PTT procedure, covalently attached chelated Gd(III) can dissociate from the nanoconstructs due to the interaction of high NIR laser power density and cause the release of free chelated Gd(III) into the bloodstream with unforeseen effects. Also, the presence of other ions (Zn, Cu, Ca) in the bloodstream has a

competing affinity to replace Gd(III) ions from the chelating molecule and thereby causes the dissociation of free Gd(III) into the bloodstream, resulting in toxicity concerns such as renal failure or nephrogenic systemic fibrosis, which is an untreatable condition.[44] In addition, free Gd(III) ions are deposited in other organs such as human brain, skin, bones, and some other vital organs. Stable ~100 nm TNPs described here provide robust methods of tracking GNRs for biodistribution and PTT dosing without the risk of toxicity and well-known size-dependent clearance pathways through the hepatobiliary system. Minimal <10 ng/g levels of Gd were detected in the kidneys and bloodstream 10 days post-therapy, and normal renal function and morphology indicate the absence of acute toxicity for these constructs. Long-term studies of clearance and renal toxicity are warranted prior to clinical translation, especially if multiple rounds of treatment are considered.

A second advance reported in this study is the dramatic increase in the efficacy of TNP delivery to CRLM tumors *via* local hepatic circulation. Systemically administered NPs result in a lower uptake (0.7% ID) at the tumor site, lowering the therapeutic efficiency and increasing the off-target effect potential.[14] Our PEGylated TNPs with optical/MR/X-ray contrasts delivered using interventional radiology techniques *via* a hepatic portal vein provide a way to increase the solid tumor dose. We demonstrated *via* MR imaging that a significantly higher NP dose (2.1×) can be obtained rapidly (~5 min) in CRLM tumors *via* local portal vein injections under interventional radiology guidance. The reliance on the Wistar rat model with a maximum weight of 400−500 g and small tumor feeding arteries introduced challenges in using arterial routes for TNP delivery and PTT while maintaining animal survival. For clinical applications, arterial delivery is feasible and even superior to portal vein routes used due to animal model constraints in this study. Although other image-guided thermal therapies such as microwave or RF ablation are important tools for treating CRLM tumors and are clinically well accepted, they are nonspecific to tumors and often result in partial tumor ablations due to unclear tumor boundaries during clinical imaging. The combination of locally delivered TNPs with NIR-light-carrying fiber-optics placed in the catheter used for delivering TNPs allows an elegant and efficient method for delivering low and safe laser power levels for specific ablation of CRLM tumors, while minimizing the off-target effects. In this proof-of-concept study, we used a 100 μm core diameter optical fiber with exposed ends; it translates into the generation of an isotropic point source of diffuse photons with an almost spherical and exponentially attenuating illumination envelope centered at the fiber tip. In the histology of a whole liver lobe, we observed almost spherical ablation zones, which covered the entire tumor, with some viable regions left at the periphery. Optimized fibers with cylindrical diffuser-equipped tips will be better to obtain a wider and more uniform illumination field for covering the entire tumor and ensure complete ablation. The optimal distance of the fiber tip from the catheter will need to be determined *via* additional experiments and computer simulations of NIR photon transport and bioheat transfer modeling. These optimizations will be explored in future work. Further, the TNPs were stable in shape and size with PTT, thus ensuring consistency in potential clearance routes from the body. Further, the reported TNPs had luminescence at 1532 nm upon 980 nm excitation (Figure 7E). The quantum yield of luminescence was low, thus restricting imaging to an intraoperative setting in the large 300−400 g rats used in the study with exposure times on the order of 5−10 s; however, with the application of further sensor

cooling and optimization of rare-earth doping on the Gd layer, additional image-guided surgery applications such as tumor margin ablation postresection can be developed. Future studies will track the long-term therapy efficacy and tumor relapse post-PTT in large liver tumor animal models such as rabbit and assess the longer-term impact of residual Au and Gd retention in viscera on liver and renal function.

MATERIALS AND METHODS

Materials.

Au(III) chloride trihydrate ($HAuCl_4 \cdot 3H_2O$, >99.9%, Fluka), CTAB (>99%, Sigma), $AgNO_3$ (ACS reagent, >99%, Sigma-Aldrich), ascorbic acid (AA, 99%, Sigma), sodium borohydride (>99%, Fluka), HCl (VWR Analytical), NaOA (>97%, TCI), HMT (>99%, Sigma-Aldrich), lanthanum nitrate hexa/pentahydrate (Ln = Gd, Yb, Er; 99.9%, Aldrich), APTES (99%, Aldrich), *N,N*-dimethylformamide (ACS reagent, DMF, VWR Analytical), methoxy-PEG_{5000}-COOH (mPEG-COOH; Nanocs, New York, NY), benzotriazol-1-yl-oxy-tris(dimethylamino)phosphonium hexafluorophosphate (BOP reagent, 97%, Aldrich), triethylamine (99%, Sigma-Aldrich), and Milli-Q water (18.2 MΩ·cm at 25 °C, Millipore) were used without further purification.

Synthesis of GNRs.

GNRs with NIR SPR properties were synthesized using a seed-mediated growth process.[37] First, Au seed particles were prepared by adding 0.5 mL of a 5 mM $HAuCl_4$ solution to 5 mL of distilled water and 5 mL of 0.2 M CTAB solution. The resulting solution was stirred, and ~0.6 mL of ice-cold $NaBH_4$ (0.1 M) was added. The seed particles were kept at room temperature. For the growth of GNRs, 1.14 mL of $AgNO_3$ solution (0.1 M) and 1.125 mL of HCl (1.2 M) were added to 450 mL of CTAB (0.2 M), and the resulting solution was vortexed for 3 min. Then, 90 mL of 0.005 M $HAuCl_4$ was added and mixed with 55.5 mL of AA (0.01 M). The color of the resulting solution became dark yellow first and immediately turned colorless. Then, 750 μL of Au seed solution was added and mixed for 20 s, and GNRs were grown for 12 h. Then, CTAB-stabilized GNRs were centrifuged at 12,000 rpm for 15 min and redispersed in distilled water. Centrifugation was performed twice, and the GNRs were dispersed in 0.02 M NaOA and heated at 80 °C for 1 h. The final concentration of NaOA−GNR was adjusted to 5×10^{11} NP/mL.

Synthesis of TNPs.

TNPs were prepared by growing a shell of Gd_2O_3:Yb/Er on NIR-resonant GNR−NaOA. For a typical synthesis of TNPs, 150 mL of GNR-NaOA (10^{11} NP/mL) was added to 450 mL of distilled water and vortexed for 3 min. Then, 1.5 mL of HMT (0.1 M) and 4.5 mL of Gd(III)-nitrate precursor having Yb/Er = 18:2% (0.01 M) were added, vortexed for 3 min, and sonicated for 30 min using a sonication probe. The resulting solution was heated at 120 °C for 3 h and then cooled to room temperature. The TNPs were left undisturbed overnight, and the transparent supernatant was carefully removed. The resulting solution was centrifuged at 3000 rpm for 5 min and redispersed in distilled water. Centrifugation was repeated two times, and the solution was redispersed in 10 mL of DMF solvent. Then, 100 μL of 10% APTES was added, and the mixture was vortexed for 3 min, followed

by heating the solvent at 80 °C for 12 h. Excess APTES was removed by centrifugation. In this manner, amine-functionalized TNPs (TNP-NH_2) were prepared. To obtain neutral TNP-mPEG, ~10^{13} NPs/mL was dispersed in 20 mL of DMF solvent with 0.1 mM of mPEG-COOH, 0.12 mM of BOP reagent, and 15 μL of triethylamine. The resulting mixture was stirred at room temperature for 12 h. The obtained neutral TNP-mPEG was dispersed in PBS and concentrated to the desired concentration and stored in a refrigerator for further use. The surface-modified TNPs were studied by dispersing NPs in 10 mM NaCl solution, and the ζ-potential was measured.

Physicochemical Characterization.

TEM imaging was performed using a HITACHI H-600 TEM operating at an acceleration voltage of 70 kV to monitor both TNP morphology and stained tissue of CRLM tumors. A drop of colloidal TNPs was placed over a carbon-coated Cu grid for TEM grid preparation. A Hitachi HD-2300 dual EDS cryo-STEM (Hitachi, Tokyo, Japan) was used to scan single-particle TNP morphology, elemental mapping, and EDS spectra at an acceleration voltage of 200 kV. The stained CRLM tissue sections were imaged with a STEM at an acceleration voltage of 120 kV. The absorption spectra of TNPs were measured using an Infinite 200 PRO (Tecan, Mannedorf, Switzerland) spectrophotometer. The hydrodynamic size *via* dynamic light scattering and ζ-potential of TNPs were measured using a Malvern Zetasizer Nano ZS (Malvern Instruments, United Kingdom) operated at 25 °C. NIR fluorescence imaging was observed by excitation of a 980 nm NIR light from both sides of a quartz test tube containing TNPs and using a 980 nm notch and 1550 ± 25 nm band-pass filters. The images were recorded using a high-speed GigE interface 640 × 532 pixel two-dimensional NIRvana:640, InGaAs array NIR/shortwave-infrared imaging camera controlled using a 64-bit LightField software. MR relaxation of TNPs was measured using a Bruker BioSpec 94/30 USR 9.4-T Preclinical MR imaging system (Bruker Biospin MRI) with a 310 mm clear warm bore. Different concentrations of TNPs were sealed in 200 μL centrifuge tubes and placed in an MR scanner. T1MR relaxation times were measured using a saturation recovery sequence called Bruker:RAREVTR using the following parameters: TE = 1.4 ms, a total of 20 TRs from 25.7 to 5000 ms (25.7, 79.4, 136.2, 196.3, 260.3, 328.6, 402, 481.3, 567.3, 661.4, 765.3, 881.3, 1012.5, 1341.6, 1558.3, 1835.4, 2219.9, 2852.9, and 5000 ms). T_2 relaxation times were acquired using a sequence protocol Bruker:MSME axial using the following parameters: TE = 1.4 ms, a total of eight echo times of 1.4, 2.8, 4.2, 7.0, 8.4, 9.8, and 11.2 ms, and TR = 2000 ms. Bruker ParaVision 6.0.1 software was used to calculate the relaxation time constants.

Cell Culture and Orthotopic Tumor Implantation.

For implantation, CC-531 cells were cultured and maintained as described earlier.[3] The CC-531 cell line (generously donated by the University of Pittsburgh) was obtained and cultured in Dulbecco's modified Eagle's medium (DMEM) (Life Technologies, Carlsbad, CA) and supplemented with 10% fetal bovine serum (Gemini Bio-Products, West Sacramento, CA) and 1% penicillin−streptomycin (Sigma-Aldrich, St. Louis, MO) in culture flasks at 37 °C and 5% CO_2. The cells were trypsinized and resuspended to achieve 5 × 10^5 cells in 200 μL of DMEM after checking the viability 30 min before implantations.

All the animal procedures were performed with the approval of institutional animal care and use committee. Subcapsular implantation of CC-531 cells was performed as described in our earlier studies.[3] Briefly, WAG/RijCmcr rats weighing 300−350 g were anesthetized by 2−3% isoflurane inhalation. The left hepatic lobe was externalized by making a 3 cm midline incision. A subcapsular injection of suspended cells was performed, and homeostasis was achieved. A two-layer closure was performed, abdominal bandage was applied, and the rats were returned to the animal facility after recovery. The tumors were grown for 7 days, and percutaneous ultrasound imaging (GE venue 20, GE Healthcare, Waukesha, WI) was performed to confirm the presence of tumors.

In Vivo Magnetic Resonance Imaging.

The rats were imaged using a GE Healthcare Discovery MR950 7.0T human MR scanner (GE Health Care, Waukesha, WI) using a commercial coil placed directly on the liver region. The animals were anesthetized using 2−3% isoflurane mixed with 100% O_2. Breathing artifacts on the images were avoided by implementing a triggered acquisition using an MRI-compatible small animal respiratory gating system (SA Instruments, Stony Brook, Inc., NY). Rectal and subcutaneous probes monitored the body temperature and electrocardiogram, respectively. Anatomical images were acquired using a 32-channel receiver coil, and standard 2D spoiled gradient recalled sequences were used for the acquisition of images (slice thickness = 1 mm; TR = 100 ms; TE = 3.072 ms; matrix = 256 × 256; flip angle = 15°). A 9.4T Bruker BioSpin MRI system was used to obtain T_1-weighted (TE = 2.4 ms and TR = 100 ms) and T_2-weighted (TE = 14.63 ms and TR = 1000 ms) images.

Catheter Placement.

Catheterization of the mesenteric vein was carried out following the general method described elsewhere.[45] The rats were placed upon an angiography table and anesthetized *via* isoflurane inhalation. A 5 cm long incision was made caudally from the xiphoid process through the fascia and linea alba. Cotton-tipped applicators were used to gently externalize the cecum and intestine to expose the mesentery. A large clearly visible mesenteric vein was selected, and the surrounding connective tissue was removed with a saline-soaked cotton tip. A small curved hemostat was used to place an 8 cm piece of saline-soaked 2–0 silk braided nonabsorbable suture (Stoelting Co., Wood Dale, IL) proximal and underneath the selected midpoint (selected site) of mesenteric vein access. Similarly, another saline-soaked 2–0 suture was placed distal to the site of mesenteric vein access. The introducer of a 24-G SurFlash polyurethane catheter (Terumo Medical Co., Somerset, NJ) was inserted into a mesenteric vein in the midpoint to visualize a flash of blood. Immediately, the introducer was removed, and the catheter was advanced. Further, a guide wire Asahi Cofianza with an outer diameter of 0.014 in. (Abbott, Abbott Park, IL) was introduced *via* the JB1, 3-French catheter (Cook Medical, Bloomington, IN) and gradually advanced into a hepatic portal vein. Once the position of the guide wire was confirmed by fluoroscopy (GE OEC 800, GE Healthcare, Waukesha, WI), the guide wire was removed, and 1 mL of saline was injected to check the potency. The hepatic vasculature was visualized by injecting 1 mL of Omnipaque (GE Healthcare, Piscataway, NJ), and digital subtracted angiography was performed by C-Arm.

TNP Infusion and Photothermal Ablation.

The TNPs were infused into the liver *via* a catheter that was placed in the liver as described above. A bolus injection of 500 μL of TNPs was carried out, followed by 1 mL of saline to flush the catheter. In the animals that needed photothermal ablation, a premeasured sterile 100 nm fiberoptic was introduced *via* a catheter. The photothermal ablation was performed with a diode fiber laser using a continuous wave of 808 nm at 0.55 W/cm^2 at the tip for 3 min (BWF5; B&W Tek, Newark, DE). An infrared thermal camera (FLIR A655sc Infrared (IR), FLIR Systems, Wilsonville, OR) was used to measure the temperature of the irradiated region.

Rotational Angiography or DynaCT Imaging.

The anesthetized rats were imaged using a ceiling-mounted Artis Zee ceiling unit with DynaCT and Inspace 3D capability (Siemens, Hoffman Estates, IL) at 80 keV energy. A 3D software was used to reconstruct the images to locate the catheter and to find the deposition of TNPs.

Histology.

After PTT application, animals were euthanized by bilateral thoracotomy. The tumor tissue samples including the irradiated area surrounded by unaltered normal tissue were excised. Some tissue samples were fixed with a solution containing 3% glutaraldehyde plus 2% paraformaldehyde in 0.1 M cacodylate buffer, pH 7.3, for TEM analysis. At necropsy, the kidneys and normal liver from animals with tumors and one with no tumor were removed and hemidissected. Both halves of each kidney were formalin fixed, sectioned, and then stained with H&E to evaluate overall histological changes.

ICP-MS Biodistribution Study.

For dried tissues (including feces and urine), nitric acid (HNO_3; 90%) and hydrogen peroxide (H_2O_2; 10%) were added and heated at 80 °C until completely dissolved. Then, the ICP-MS sample of each tissue composed of 3% (by volume) of the dissolved tissue and the rest diluted with distilled water was used to determine the metal content per gram of tissue.

Supplementary Material

Refer to Web version on PubMed Central for supplementary material.

ACKNOWLEDGMENTS

Financial support was provided by NIH R01 CA193343, MCW Cancer Center (WBCS), and MCW Center for Imaging Research, Radiology, to M.J.F.; Alliance for Healthy Wisconsin, Rock River Cancer Research Foundation (RRCRF), and MCW Research Affairs Committee (RAC) Pilot Grant to A.J.; Institutional Research Grant No. 86–004-26 from the American Cancer Society and RSNA Research Scholar Grant to S.B.W.; and NIH R01 CA218144 to P.S.L. This work was also supported by a grant from The Medical College of Wisconsin Cancer Center and Dr. Nancy Sobczak Fund for Breast Cancer. We thank Dr. El-Sayed H. Ibrahim, Department of Radiology for helping in MR imaging.

REFERENCES

(1). American Cancer Society. Colorectal Cancer Facts & Figures 2017−2019; American Cancer Society: Atlanta, 2017.

(2). Siegel RL; Miller KD; Fedewa SA; Ahnen DJ; Meester RGS; Barzi A; Jemal A. Colorectal Cancer Statistics. Ca-Cancer J. Clin. 2017, 67, 177–193. [PubMed: 28248415]

(3). White SB; Procissi D; Chen J; Gogineni VR; Tyler P; Yang Y; Omary RA; Larson AC Characterization of CC-531 as a Rat Model of Colorectal Liver Metastases. PLoS One 2016, 11, e0155334.

(4). Fernandez FG; Drebin JA; Linehan DC; Dehdashti F; Siegel BA; Strasberg SM Five-year Survival After Resection of Hepatic Metastases from Colorectal Cancer in Patients Screened by Positron Emission Tomography with F-18 Fluorodeoxyglucose (FDG-PET). Ann. Surg. 2004, 240, 438–450. [PubMed: 15319715]

(5). Vigano L; Russolillo N; Ferrero A; Langella S; Sperti E; Capussotti L. Evolution of Long-term Outcome of Liver Resection for Colorectal Metastases: Analysis of Actual 5-year Survival Rates Over Two Decades. Ann. Surg. Oncol 2012, 19, 2035–2044. [PubMed: 22219066]

(6). Beg MS; Adhami F; Xuan L; Hodges J; Meyer J; Halm E; Pruitt S. Liver-directed Therapies for Colorectal Cancer Liver Metastasis (CLRM): A Surveillance, Epidemiology, and End Results (SEER)-Medicare Analysis. J. Clin. Oncol. 2014, 32, 577–577.

(7). Scheffer HJ; Vroomen LG; Nielsen K; van Tilborg AA; Comans EF; van Kuijk C; van der Meijs BB; van den Bergh J; van den Tol PM; Meijerink MR Colorectal Liver Metastatic Disease: Efficacy of Irreversible Electroporation—A Single-arm Phase II Clinical Trial (COLDFIRE-2 Trial). BMC Cancer 2015, 15, 772. [PubMed: 26497813]

(8). Valerio M; Dickinson L; Ali A; Ramachandran N; Donaldson I; Freeman A; Ahmed HU; Emberton M. A Prospective Development Study Investigating Focal Irreversible Electroporation in Men with Localised Prostate Cancer: Nanoknife Electroporation Ablation Trial (NEAT). Contemp. Clin. Trials 2014, 39, 57–65. [PubMed: 25072507]

(9). Konopke R; Roth J; Volk A; Pistorius S; Folprecht G; Zophel K; Schuetze C; Laniado M; Saeger HD; Kersting S. Colorectal Liver Metastases: An Update on Palliative Treatment Options. J. Gastrointestin. Liver Dis. 2012, 21, 83–91. [PubMed: 22457864]

(10). Bardhan R; Lal S; Joshi A; Halas NJ Theranostic Nanoshells: From Probe Design to Imaging and Treatment of Cancer. Acc. Chem. Res. 2011, 44, 936–946. [PubMed: 21612199]

(11). Janib SM; Moses AS; MacKay JA Imaging and Drug Delivery Using Theranostic Nanoparticles. Adv. Drug Delivery Rev. 2010, 62, 1052–1063.

(12). Park K. To PEGylate or Not to PEGylate, That Is Not the Question. J. Controlled Release 2010, 142, 147–148.

(13). Bae YH; Park K. Targeted Drug Delivery to Tumors: Myths, Reality and Possibility. J. Controlled Release 2011, 153, 198–205.

(14). Wilhelm S; Tavares AJ; Dai Q; Ohta S; Audet J; Dvorak HF; Chan WCW Analysis of Nanoparticle Delivery to Tumours. Nat. Rev. Mater. 2016, 1, 16014.

(15). Tsoi KM; MacParland SA; Ma XZ; Spetzler VN; Echeverri J; Ouyang B; Fadel SM; Sykes EA; Goldaracena N; Kaths JM; Conneely JB; Alman BA; Selzner M; Ostrowski MA; Adeyi OA; Zilman A; McGilvray ID; Chan WC Mechanism of Hard-nanomaterial Clearance by the Liver. Nat. Mater. 2016, 15, 1212–1221. [PubMed: 27525571]

(16). MacParland SA; Tsoi KM; Ouyang B; Ma XZ; Manuel J; Fawaz A; Ostrowski MA; Alman BA; Zilman A; Chan WC; McGilvray ID Phenotype Determines Nanoparticle Uptake by Human Macrophages from Liver and Blood. ACS Nano 2017, 11, 2428–2443. [PubMed: 28040885]

(17). Tian M; Lu W; Zhang R; Xiong C; Ensor J; Nazario J; Jackson J; Shaw C; Dixon KA; Miller J; Wright K; Li C; Gupta S. Tumor Uptake of Hollow Gold Nanospheres After Intravenous and Intra-arterial Injection: PET/CT Study in a Rabbit VX2 Liver Cancer Model. Mol. Imaging Biol. 2013, 15, 614–624. [PubMed: 23608932]

(18). Li J; Zhou M; Liu F; Xiong C; Wang W; Cao Q; Wen X; Robertson JD; Ji X; Wang YA; Gupta S; Li C. Hepatocellular Carcinoma: Intra-arterial Delivery of Doxorubicinloaded Hollow Gold

Nanospheres for Photothermal Ablation-Chemoembolization Therapy in Rats. Radiology 2016, 281, 427–435. [PubMed: 27347765]

(19). White SB; Kim DH; Guo Y; Li WG; Yang YH; Chen J; Gogineni VR; Larson AC Biofunctionalized Hybrid Magnetic Gold Nanoparticles as Catalysts for Photothermal Ablation of Colorectal Liver Metastases. Radiology 2017, 285, 809–819. [PubMed: 28707960]

(20). Niekel MC; Bipat S; Stoker J. Diagnostic Imaging of Colorectal Liver Metastases with CT, MR Imaging, FDG PET, and/or FDG PET/CT: A Meta-analysis of Prospective Studies Including Patients who have not Previously Undergone Treatment. Radiology 2010, 257, 674–684. [PubMed: 20829538]

(21). Bardhan R; Chen W; Bartels M; Perez-Torres C; Botero MF; McAninch RW; Contreras A; Schiff R; Pautler RG; Halas NJ; Joshi A. Tracking of Multimodal Therapeutic Nanocomplexes Targeting Breast Cancer. Nano Lett. 2010, 10, 4920–4928. [PubMed: 21090693]

(22). Cai H; Li K; Li J; Wen S; Chen Q; Shen M; Zheng L; Zhang G; Shi X. Dendrimer-Assisted Formation of Fe3O4/Au Nanocomposite Particles for Targeted Dual Mode CT/MR Imaging of Tumors. Small 2015, 11, 4584–4593. [PubMed: 26061810]

(23). Wang L; Luo J; Fan Q; Suzuki M; Suzuki IS; Engelhard MH; Lin Y; Kim N; Wang JQ; Zhong CJ Monodispersed Core-shell Fe3O4@Au Nanoparticles. J. Phys. Chem. B 2005, 109, 21593−21601.

(24). Yang D; Yang G; Gai S; He F; An G; Dai Y; Lv R; Yang P. Au25 Cluster Functionalized Metal-organic Nanostructures for Magnetically Targeted Photodynamic/photothermal Therapy Triggered by Single Wavelength 808 nm Near-infrared Light. Nanoscale 2015, 7, 19568−19578.

(25). Rotz MW; Culver KS; Parigi G; MacRenaris KW; Luchinat C; Odom TW; Meade TJ High Relaxivity Gd(III)-DNA Gold Nanostars: Investigation of Shape Effects on Proton Relaxation. ACS Nano 2015, 9, 3385–3396. [PubMed: 25723190]

(26). Alric C; Taleb J; Le Duc G; Mandon C; Billotey C; Le Meur-Herland A; Brochard T; Vocanson F; Janier M; Perriat P; Roux S; Tillement O. Gadolinium Chelate Coated Gold Nanoparticles as Contrast Agents for both X-ray Computed Tomography and Magnetic Resonance Imaging. J. Am. Chem. Soc. 2008, 130, 5908–5915. [PubMed: 18407638]

(27). Moriggi L; Cannizzo C; Dumas E; Mayer CR; Ulianov A; Helm L. Gold Nanoparticles Functionalized with Gadolinium Chelates as High-relaxivity MRI Contrast Agents. J. Am. Chem. Soc. 2009, 131, 10828−10829.

(28). Nicholls FJ; Rotz MW; Ghuman H; MacRenaris KW; Meade TJ; Modo M. DNA-gadolinium-gold Nanoparticles for In Vivo T1MR Imaging of Transplanted Human Neural Stem Cells. Biomaterials 2016, 77, 291–306. [PubMed: 26615367]

(29). Coughlin AJ; Ananta JS; Deng N; Larina IV; Decuzzi P; West JL Gadolinium-conjugated Gold Nanoshells for Multimodal Diagnostic Imaging and Photothermal Cancer Therapy. Small 2014, 10, 556–565. [PubMed: 24115690]

(30). Hitomi E; Simpkins AN; Luby M; Latour LL; Leigh RJ; Leigh R. Blood-Ocular Barrier Disruption in Patients with Acute Stroke. Neurology 2018, 90, e915–e923. [PubMed: 29438039]

(31). Marangoni VS; Neumann O; Henderson L; Kaffes CC; Zhang H; Zhang R; Bishnoi S; Ayala-Orozco C; Zucolotto V; Bankson JA; Nordlander P; Halas NJ Enhancing T1Magnetic Resonance Imaging Contrast with Internalized Gadolinium(III) in a Multilayer Nanoparticle. Proc. Natl. Acad. Sci. U. S. A. 2017, 114, 6960–6965. [PubMed: 28630340]

(32). Wu WC; Tracy JB Large-Scale Silica Overcoating of Gold Nanorods with Tunable Shell Thicknesses. Chem. Mater. 2015, 27, 2888–2894. [PubMed: 26146454]

(33). Wang JH; Huang H; Zhang DQ; Chen M; Zhang YF; Yu XF; Zhou L; Wang QQ Synthesis of Gold/rare-earth-vanadate Core/shell Nanorods for Integrating Plasmon Resonance and Fluorescence. Nano Res. 2015, 8, 2548–2561.

(34). Guo T; Lin Y; Li Z; Chen S; Huang GM; Lin HR; Wang J; Liu G; Yang HH Gadolinium oxysulfide-coated Gold Nanorods with Improved Stability and Dual-modal Magnetic Resonance/photoacoustic Imaging Contrast Enhancement for Cancer Theranostics. Nanoscale 2017, 9, 56–61. [PubMed: 27906396]

(35). Song Y; Liu GX; Dong XT; Wang JX; Yu WS; Li JM Au Nanorods@NaGdF4/Yb3+,Er3+ Multifunctional Hybrid Nanocomposites with Upconversion Luminescence, Magnetism, and Photothermal Property. J. Phys. Chem. C 2015, 119, 18527−18536.

(36). Harris-Birtill D; Singh M; Zhou Y; Shah A; Ruenraroengsak P; Gallina ME; Hanna GB; Cass AEG; Porter AE; Bamber J; Elson DS Gold Nanorod Reshaping In Vitro and In Vivo Using a Continuous Wave Laser. PLoS One 2017, 12, e0185990.

(37). Nikoobakht B; El-Sayed MA Preparation and Growth Mechanism of Gold Nanorods (NRs) Using Seed-Mediated Growth Method. Chem. Chem. Mater. 2003, 15, 1957–1962.

(38). Taylor AB; Siddiquee AM; Chon JW Below melting point photothermal reshaping of single gold nanorods driven by surface diffusion. ACS Nano 2014, 8, 12071−12079.

(39). Ayala-Orozco C; Urban C; Knight MW; Urban AS; Neumann O; Bishnoi SW; Mukherjee S; Goodman AM; Charron H; Mitchell T; Shea M; Roy R; Nanda S; Schiff R; Halas NJ; Joshi A. Au Nanomatryoshkas as Efficient Near-infrared Photothermal Transducers for Cancer Treatment: Benchmarking Against Nanoshells. ACS Nano 2014, 8, 6372–6381. [PubMed: 24889266]

(40). Maestro LM; Haro-Gonzalez P; Sanchez-Iglesias A; Liz-Marzan LM; Garcia Sole J; Jaque D. Quantum Dot Thermometry Evaluation of Geometry Dependent Heating Efficiency in Gold Nanoparticles. Langmuir 2014, 30, 1650–1658. [PubMed: 24495155]

(41). Moghadam FF Using Nanoparticles in Medicine for Liver Cancer Imaging. Oman Med. J. 2017, 32, 269–274. [PubMed: 28804578]

(42). An SSA; Lee J-A; Kim M-K; Paek H-J; Kim Y-R; Kim M-K; Lee J-K; Jeong J; Choi S-J Tissue Distribution and Excretion Kinetics of Orally Administered Silica Nanoparticles in Rats. Int. J. Nanomed. 2014, 9, 251–260.

(43). Qin H; Zhou T; Yang S; Chen Q; Xing D. Gadolinium(III)-gold Nanorods for MRI and Photoacoustic Imaging Dual-modality Detection of Macrophages in Atherosclerotic Inflammation. Nanomedicine 2013, 8, 1611–1624. [PubMed: 23351094]

(44). Rogosnitzky M; Branch S. Gadolinium-based Contrast Agent Toxicity: A Review of Known and Proposed Mechanisms. BioMetals 2016, 29, 365–376. [PubMed: 27053146]

(45). Sheu AY; Zhang Z; Omary RA; Larson AC Invasive Catheterization of the Hepatic Artery for Preclinical Investigation of Liver-directed Therapies in Rodent Models of Liver Cancer. Am. J. Transl. Res. 2013, 5, 269–278. [PubMed: 23634238]

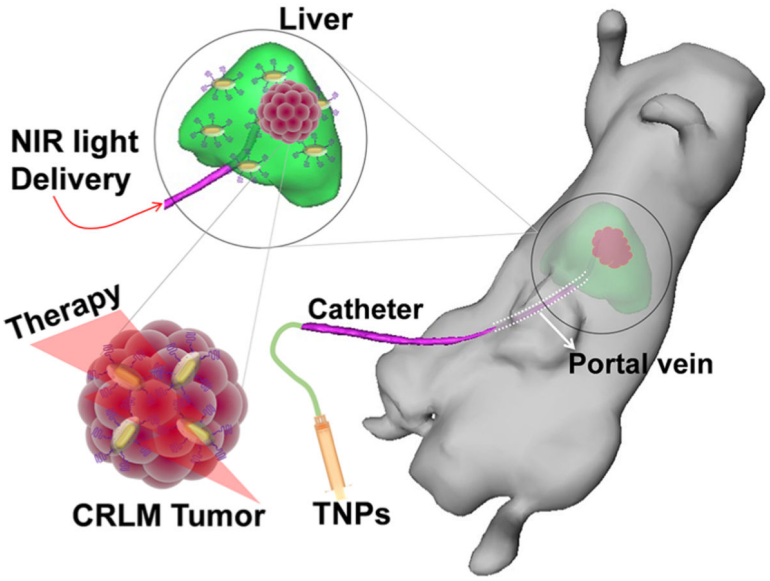

Figure 1.
Schematic illustrating the site-selective delivery of TNPs *via* the hepatic portal vein and PTT using a catheter-based 808 nm NIR laser.

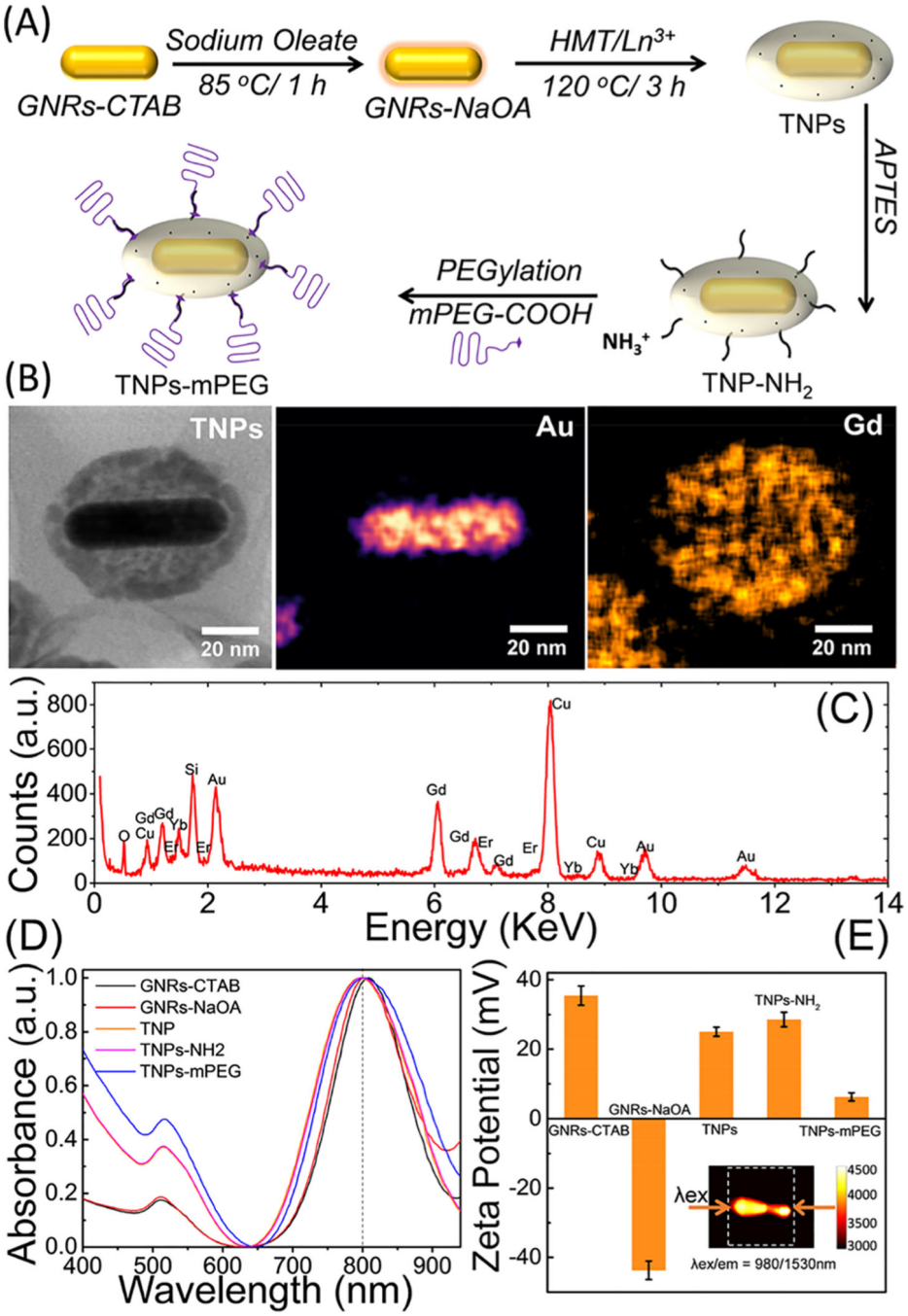

Figure 2.

Synthesis and characterization of TNPs. (A) Schematic for the synthesis of TNPs. (B) STEM image demonstrating the morphology of TNPs and Au/Gd elemental mapping. (C) EDS spectrum for different elements comprising TNPs. (D) UV−visible spectra of NPs in sequential stages of the synthesis and the corresponding ζ-potential changes in (E). Inset of (E) depicts the second NIR window (NIR-II) downconversion emission of TNPs at 1530 nm upon excitation using two 980 nm diode lasers (200 mW) from both sides of a 1 mL quartz cuvette.

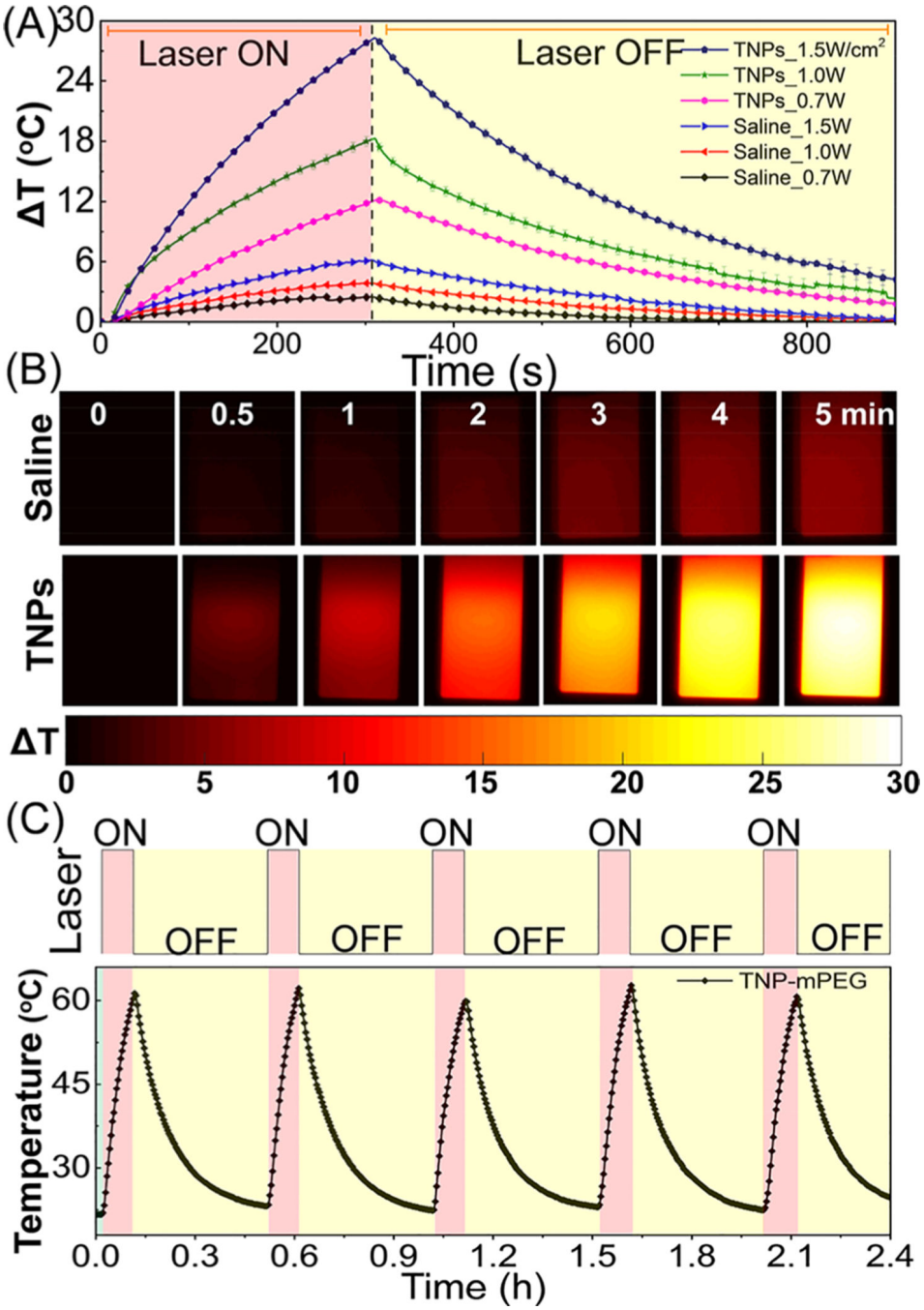

Figure 3.

Photothermal studies of TNPs. (A) Temperature kinetics of both saline and TNP-mPEG phantom models irradiated for 3 min using an NIR laser diode at 808 nm, followed by cooling for 10 min at different surface power densities. (B) FLIR thermal images of a cuvette containing saline or TNPs at selected time points between 0 and 5 min at 1.5 W/cm^2 irradiation. (C) Temperature cycling stability of TNP-mPEG at 2 W/cm^2 irradiation for five laser ON/OFF cycles.

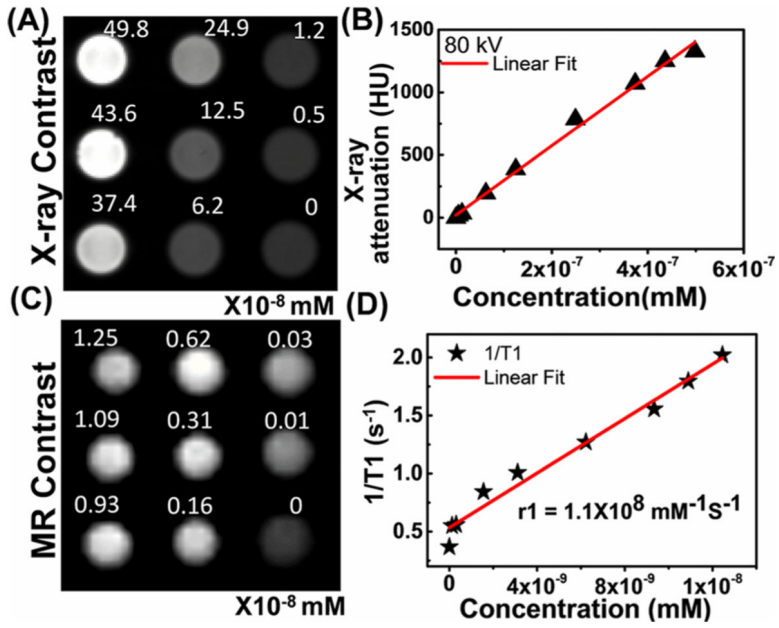

Figure 4.

(A) *In vitro* CT phantom slice consisting of different concentrations of TNPs at 80 kV. (B) Measured X-ray attenuation number (in HU units) with different concentrations of TNPs. (C) *In vitro* T_1-weighted MR phantom slice consisting of different concentrations of TNPs dispersed in water and (D) its T_1 relaxivity per NP.

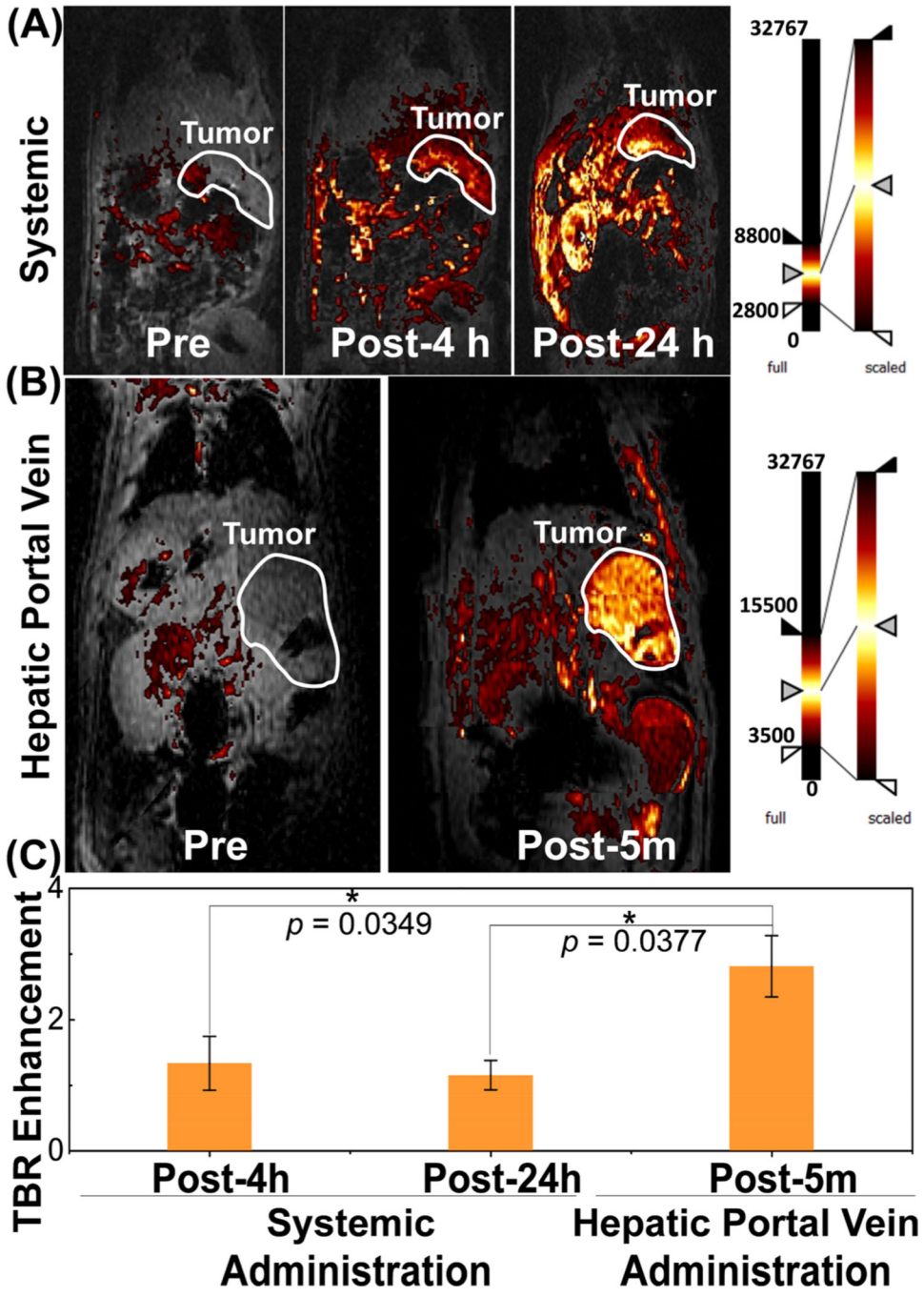

Figure 5.

T_1 contrast MR imaging by systematic and site-selective delivery of TNPs in a CRLM rat model. Monitoring *in vivo* T_1-weighted MR images of rats with CRLM tumor for (A) pre- (0 h), post-4 h, and post-24 h tail vein injection and (B) pre- and post-5 min portal vein injection of TNP. Tumor is shown in the white outline. (C) Tumor-to-background ratio enhancement comparison of CRLM tumors between tail vein injection and portal vein injection ($n = 3$, $^*p < 0.05$).

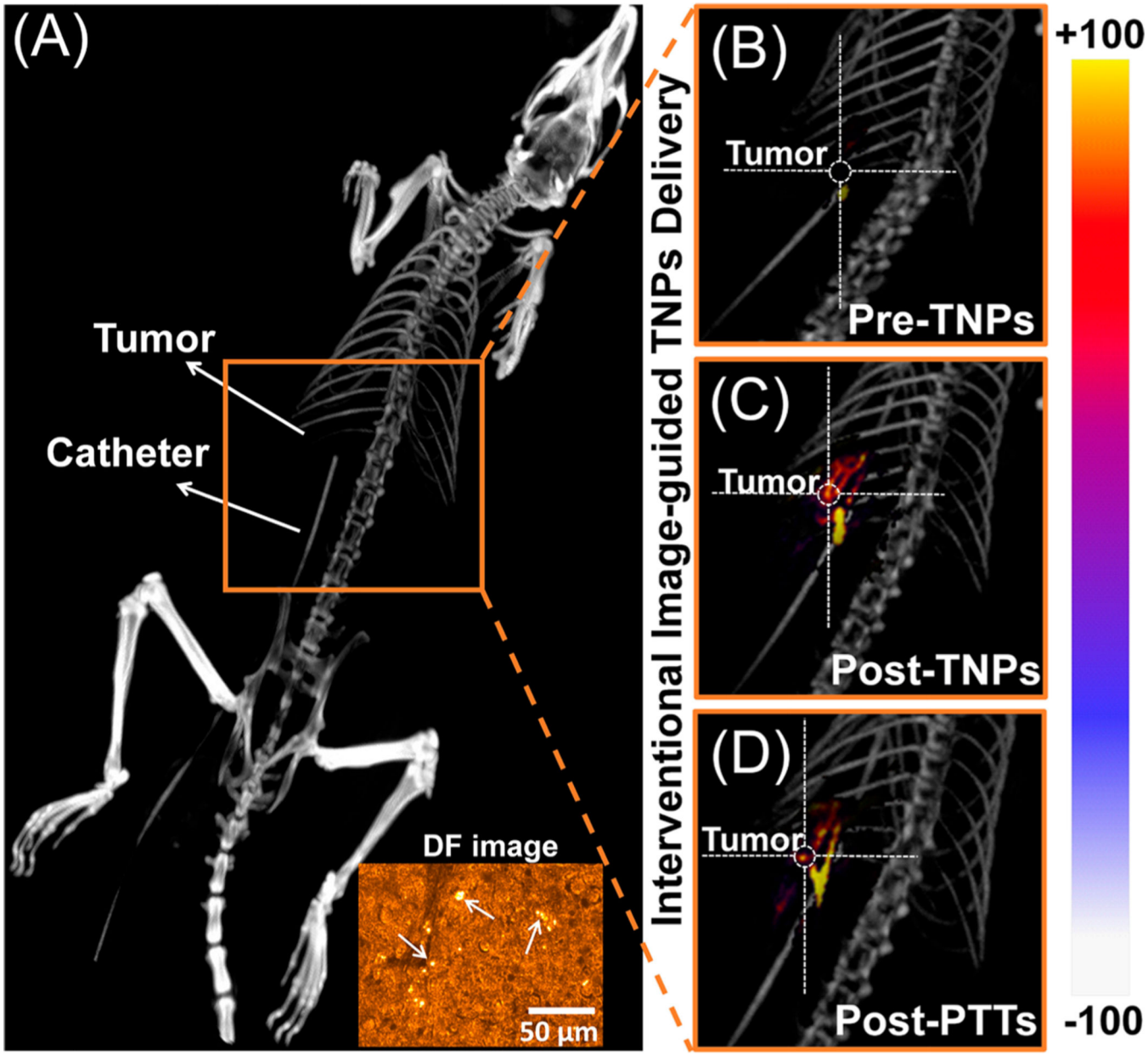

Figure 6.

Interventional image-guided TNP delivery and therapy. (A) 3D reconstructions of DynaCT image of a rat with a CRLM tumor, where the catheter was placed in the liver *via* a portal vein. Rats were injected with TNPs followed by saline. DynaCT image of rats (B) pre-TNPs, (C) post-TNPs, and (D) post-PTT. Inset of (A) shows the dark-field image of CRLM tumor tissue having TNPs; pointed arrows indicate scattering from TNPs.

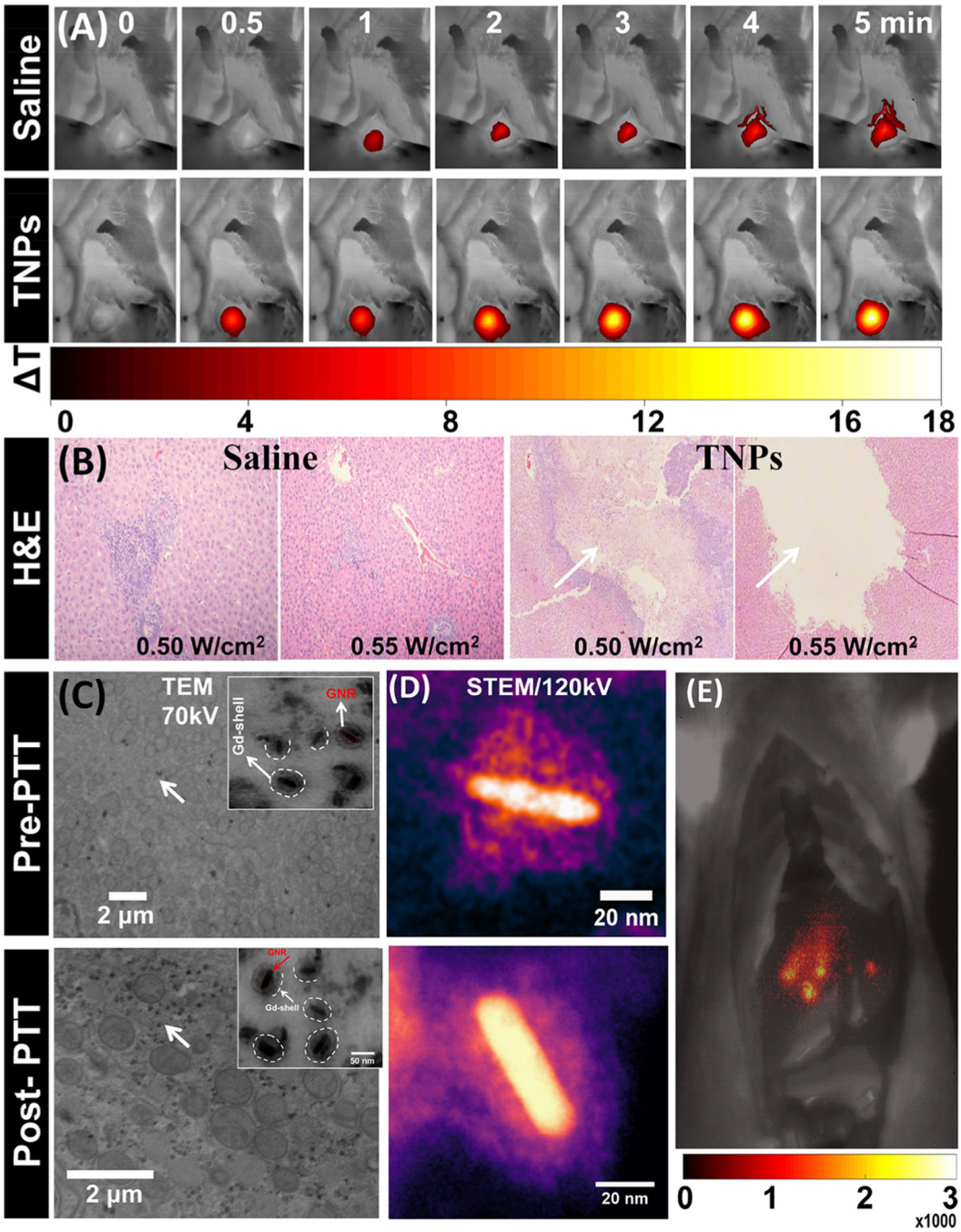

Figure 7.

In vivo PTT with saline and TNP-treated rats. (A) FLIR thermal images of CRLM tumor-bearing rats on site-selective delivery of TNPs and saline, irradiated with an 808 nm NIR laser at 0.55 W/cm^2 at 0, 0.5, 1, 2, 3, 4, and 5 min time points. (B) Representative histological images of saline and TNP-ablated (at 0.50 and 0.55 W/cm^2) CRLM tumor tissue stained with H&E. Pre-PTT (without PTT) and post-PTT (with PTT) CRLM tissue images acquired using (C) TEM at 70 kV and (D) STEM at 120 kV, confirming the undisturbed core/shell structure of TNPs. (E) SWIR emission monitoring from CRLM rat 980 nm

excitation and 1550 ± 25 nm emission with 10 s exposure after local injection of 50 μL of TNP solution (10^{12} TNPs/mL concentration).

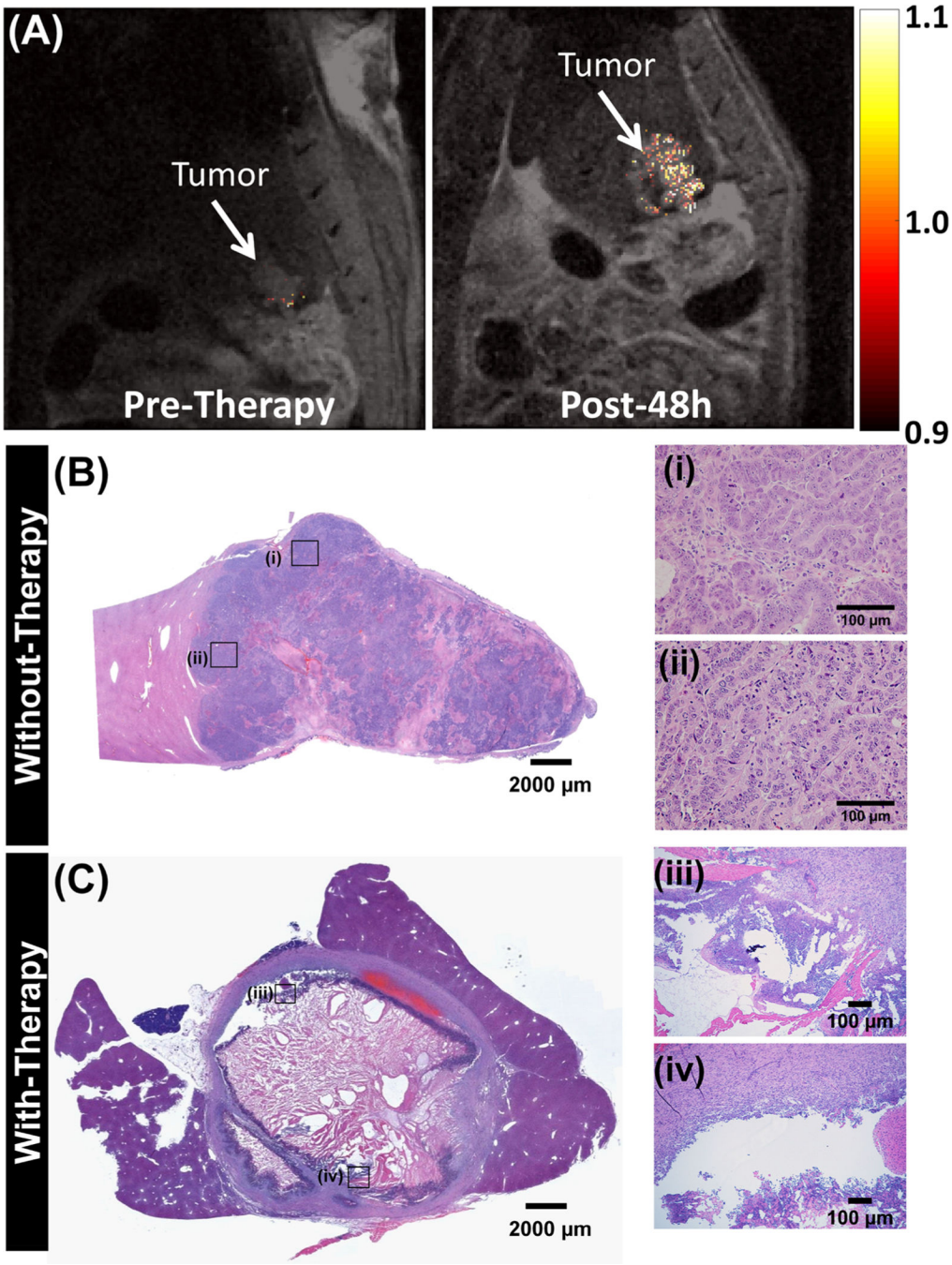

Figure 8.

In vivo hepatic portal vein T_1/T_2 MR imaging at pre- and post-therapy. (A) Representative 9.4 T T_1-weighted coronal MR images of the tumor contrast in CRLM tumor-bearing rats overlaid onto T_2-weighted MR images for pre- and post-48 h therapy. Enhancement in mean tumor T_1 contrast at pre- and post-48 h calculated for $n = 3$ rats. Representative H&E images of tumors in (B) untreated animals. The images (i and ii) on the right side show the enlarged rectangular region on the left panel. (C) TNPs and laser, where a large necrotic region is visible in the center of the tumor, and peripheral regions are characterized by apoptotic cells.

The images (iii and iv) on the right side show the enlarged rectangular region on the left panel, where the disintegrated tumor region is clearly visible.

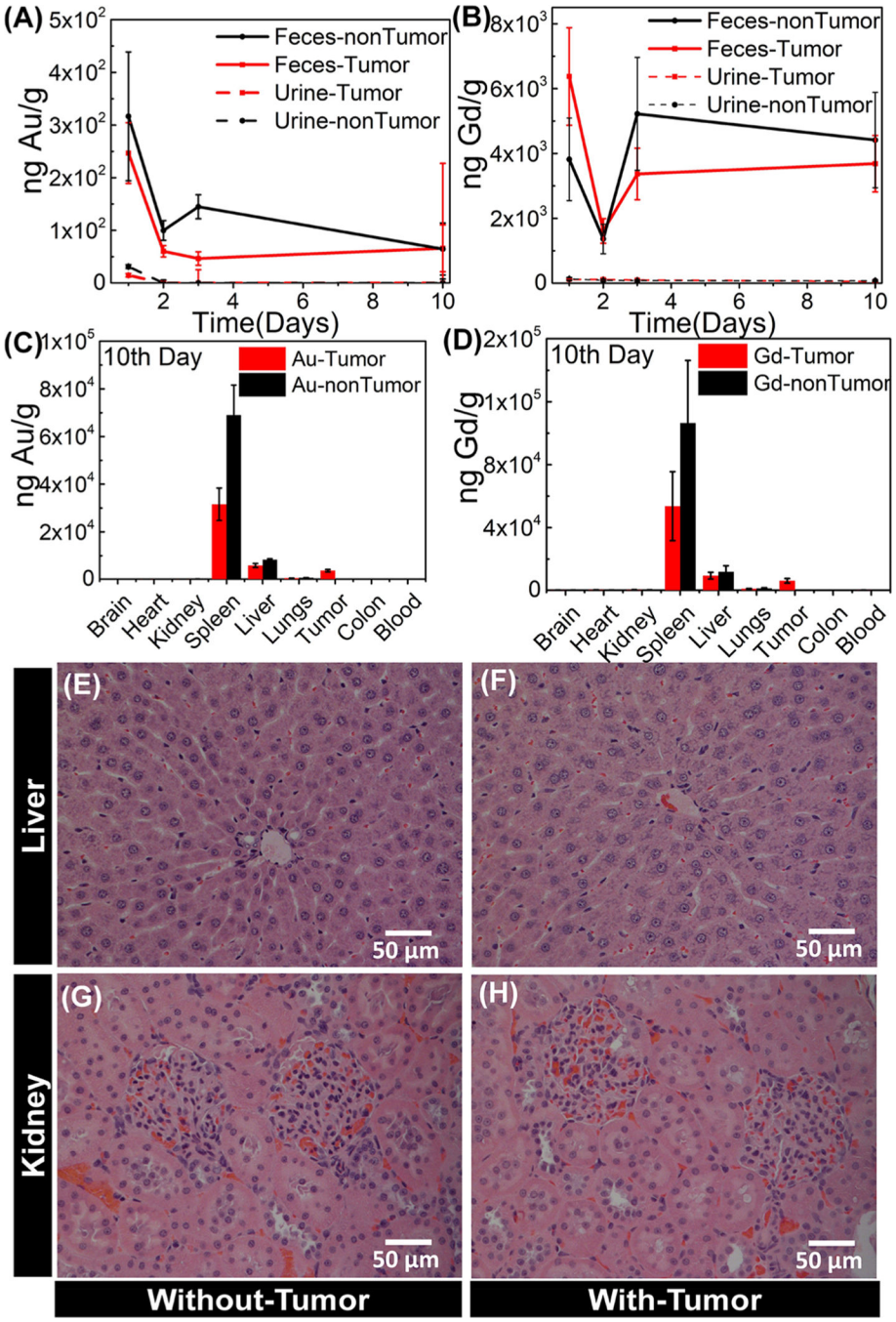

Figure 9.

Biodistribution kinetics and clearance of TNPs using ICP-MS and H&E staining of livers and kidneys. Biodistribution kinetics of Au and Gd in (A,B) feces (solid lines) and urine (dotted lines) until the 10th day of TNP postadministration, (C,D) accumulation in major organs of the rats at the 10th day of TNP postsystemic administration in both CRLM tumor-bearing (n = 6 rats/group) and non-tumor-bearing (n = 3 rats/group) rats (error bars represents mean ± SEM). Representative H&E-stained images of the liver from the (E) non-tumor-bearing and (F) tumor-bearing animal show no damage in hepatocytes at the 10th

day of TNP postsystemic administration. Representative H&E-stained images of the kidneys from the (G) non-tumor-bearing and (H) tumor-bearing animal show normal glomerulus.